

Full-Space Scanning Periodic Phase-Reversal Leaky-Wave Antenna

Ning Yang, *Member, IEEE*, Christophe Caloz, *Fellow, IEEE*, and Ke Wu, *Fellow, IEEE*

Abstract—A novel full-space scanning periodic phase-reversal leaky-wave antenna array is proposed, designed in offset parallel stripline technology, and demonstrated experimentally. This antenna radiates from its small phase-reversing cross-overs, which leads to a small leakage factor and subsequently a large directivity. The operation principle of the antenna is explained from the Brillouin diagram, which shows how single-beam scanning, using the $m = -1$ space harmonic, is achieved as a result of the π lateral shift of the dispersion curves due to phase reversal. One of the benefits of phase reversal is to permit this radiation performance with relatively small permittivity substrates ($\epsilon_{e,\min} = 4$ compared to $\epsilon_{e,\min} = 9$ for antennas without phase reversal). A unit-cell matching technique is applied to avoid reflections, and thereby prevent the presence of an open stopband so as to permit continuous space scanning with efficient broadside radiation. An efficient array synthesis procedure, based on a transmission line modeling of the structure, is utilized for the design of the antenna following specifications in terms of frequency, scanning, directivity, radiation efficiency, and sidelobe level. A uniform-aperture antenna prototype, including a balun-transformer input transition, is presented, featuring experimental beamwidth and gain at the broadside frequency (25 GHz) of 4° and 15.7 dBi, respectively.

Index Terms—Balanced transmission line, full-space scanning, leaky-wave antenna, millimeter wave, offset parallel stripline (OPS), open stopband, phase reversal, planar antenna.

I. INTRODUCTION

TRAVELING-WAVE antennas are antennas supporting wave propagation in a unique direction [1], [2]. When the wave has a phase velocity smaller than the speed of light (slow wave), the antenna structure guides the wave along its axis and radiates it from its end. It is a surface-wave antenna and it generally produces endfire radiation [3]. Surface-wave antennas include long wires, dielectric rods, and helices [3]. In contrast, when the wave has a phase velocity larger than the speed of light (fast wave), the antenna structure progressively radiates the wave from its input to its end. It is a leaky-wave antenna and its beam may be steered to different angles of space by tuning the frequency [4]. Slotted waveguides [5], [6], higher order mode microstrips [7]–[10], and composite right/left-handed structures [11] belong to this family. Leaky-wave antennas, thanks to their high directivity and simple feeding structure, are

suitable for various scanning applications, such as radar and multiple-input multiple-output (MIMO) systems. They may also incorporate tunable elements, such as varactors, to provide beam steering at a fixed frequency [12] or active elements for beam shaping [13].

Planar periodic leaky-wave antennas have been intensively investigated due to their low profile, low cost, and ease of fabrication. Most of them are implemented in microstrip technology such as the comb-line array, periodic meandered microstrip array [14], and series-resonant patch array [15]. A fundamental problem of these antennas has been the existence of an open stopband in a narrow frequency region around broadside. This stopband may be understood in terms of coupling between space harmonics, or equivalently, in terms of the constructive interferences from the reflections occurring at the periodic loads. Within the stopband, the radiation efficiency abruptly drops and most of the signal is reflected back to the source [4]. Traditionally, such antennas have been mostly considered as serially fed arrays of individual radiating elements periodically loading the structure [14], [16]. Only recently, they have been investigated theoretically in terms of leaky-wave structures with novel insights and design approaches [17], and the techniques to close the open stopband of a periodic microstrip comb-line leaky-wave antennas for broadside radiation is presented in [18].

This paper presents a full-space scanning leaky-wave antenna using periodic phase-reversal radiating elements interconnected by balanced transmission line sections. The phase-reversal elements have a fourfold function: ensuring the continuity of the transmission line, providing a periodic perturbation to generate space harmonics, radiating, and 180° phase shifting for single-beam operation. The periodic phase reversal inverses the phase between the two conductors of the structure in each unit cell, and thereby laterally shift the dispersion curves by π [19]–[21]. The resulting antenna may be interpreted to operate either in the $n = -1$ space harmonic or in the $n = 0$ space harmonic. The phase reversal allows single-beam frequency scanning with relatively small permittivity substrates ($\epsilon_{e,\min} = 4$ compared to $\epsilon_{e,\min} = 9$ for antennas without phase reversal). This antenna has its radiators directly in the phase reversals, which is in continuity of the balanced transmission line. As a consequence, they induce minima reflections and also lead to small leakage factor and a large directivity. Moreover, these minor discontinuities can be easily matched within each unit cell so as to totally suppress the open stopband, utilizing an unit-cell matching technique, which is similar to that adopted in [18]. The suppression of stopband ensures efficient broadside radiation and continuous beam scanning with frequency. The synthesis procedure

Manuscript received May 14, 2010; revised July 04, 2010; accepted July 19, 2010. Date of publication September 09, 2010; date of current version October 13, 2010.

The authors are with the École Polytechnique de Montréal, Montréal, QC, Canada H3T 1J4 (e-mail: n.yang@polymtl.ca).

Color versions of one or more of the figures in this paper are available online at <http://ieeexplore.ieee.org>.

Digital Object Identifier 10.1109/TMTT.2010.2065890

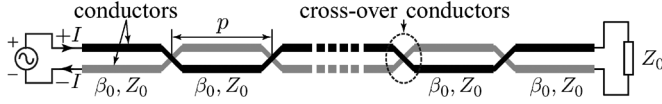


Fig. 1. Overall configuration of the proposed full-space scanning phase-reversal leaky-wave antenna. For the specific offset parallel stripline (OPS) implementation presented in this paper, the two colors (black and gray) indicate different metal strip layers, which are placed at each side of a thin substrate.

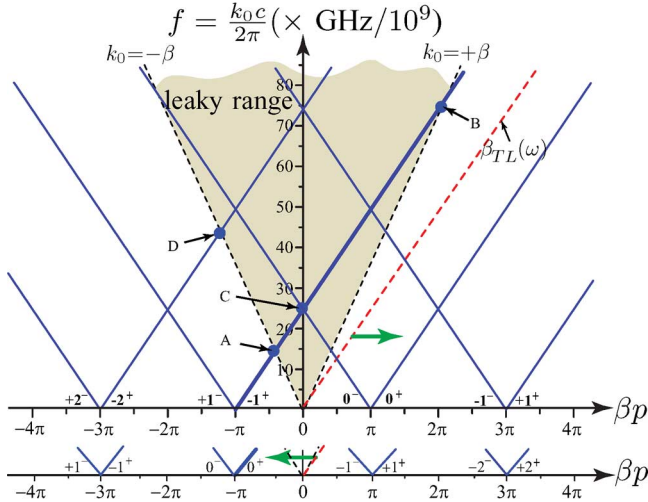


Fig. 2. Dispersion diagram obtained from (2) for the phase-reversal antenna structure shown in Fig. 1 for the parameters $\epsilon_e = 2.2$ and $p = 4.1$ mm. The shading area represents the fast-wave (radiation) region. The dispersion curve for the corresponding TEM transmission line without phase reversals (red dotted curve in online version) is also shown for reference. The upper abscissa axis represents the case of a rightward (phase delay) shift of the dispersion diagram (convention followed in this paper), corresponding to radiation of the $m = -1$ space harmonic, while the lower abscissa axis represents the case of a leftward (phase advance) shift of the dispersion diagram, corresponding to radiation of the $m = 0$ space harmonic.

of the proposed phase-reversal antenna is presented and an antenna with uniform aperture distribution is designed, fabricated, and measured.

II. PRINCIPLE OF OPERATION

Fig. 1 shows the overall configuration of the proposed full-space scanning phase-reversal leaky-wave antenna. The structure is composed of a plurality of balanced transmission line sections periodically interconnected by cross-over conductors with a period of p . All the transmission line sections have the same characteristic impedance Z_0 and **phase constant β_{TL}** . The cross-overs exchange the relative positions of the two conductors of the balanced transmission line and thereby reverse their polarity. The antenna is fed at one end through a standard balanced transmission line and is terminated at the other end by a matched (Z_0) load.

Without the phase-reversal cross-overs, the structure is merely a uniform TEM transmission line, which exhibits a linear dispersion curve, starting from the origin ($k_0 = \beta = 0$) of the dispersion diagram, as shown by the red dotted curve (in online version) in Fig. 2. It is a purely guiding (nonradiative) slow-wave structure.

The periodic phase reversals transform the structure into a periodic structure. Since the cross-overs are merely very short

transmission line sections, introducing only minor impedance discontinuities, and because the unit cells will be further internally matched so as to fully suppresses local reflections (Section III), the structure will be seen by the waves as essentially continuous. Therefore, it is *de facto* a periodic structure with a vanishingly small periodic perturbation, and it therefore **exhibits a dispersion diagram whose stopband widths collapse to zero** (because of the negligible coupling between the space harmonics due to the negligible discontinuities) and the dispersion curves collapse into a diamond-like dispersion diagram constituted of perfectly linear space harmonic curves [19], as shown in Fig. 2.

Applying periodic boundary condition, the phasor waveform along the structure may be written

$$\psi(z) = \psi_0 e^{-j\beta(\omega)z} = \psi(z - np) e^{-j\beta(\omega)np}, \quad n \in \mathbb{N}. \quad (1)$$

Using Bloch–Floquet’s theorem [19], [22], the wave in a periodic structure consists of the superposition of an infinite number of space harmonics waves, and the phase constants β_m of the m th space harmonic is given by

$$\beta_m(\omega) = \pm \left[\beta_0(\omega) + \frac{2\pi m}{p} \right], \quad m = 0, \pm 1, \pm 2, \dots \quad (2)$$

In this relation, it is assumed that $\beta_0(\omega) = \beta_{TL}(\omega) > 0$ so that the positive and negative signs correspond to waves propagating along the positive (forward- v_g) and negative (backward- v_g) z -directions, respectively, of the selected coordinate system, assuming the time dependence $e^{+j\omega t}$.

Fig. 2 shows the complete dispersion diagram for the phase-reversal structure of Fig. 1. This diagram differs from that of the most common periodic structures with a vanishingly small periodic perturbation [19], [23]. The phase reversal induced in each unit cell generates an extra frequency-independent π phase shift per cell. This results in a horizontal shifting of the entire dispersion diagram by an amount of π . Furthermore, due to the small electrical size of the phase-reversing cross-overs (tends to be zero ideally), the sign of the phase shift may be arbitrarily chosen as positive (phase delay) or negative (phase advance). Therefore, all the dispersion curves are shifted, without changing their slope ($\partial\omega/\partial\beta = v_g$), either to the right or to the left of the dispersion diagram, as illustrated in Fig. 2. In the following, we will follow the convention of Hessel [19], where the phase reversals are considered as phase delays and the dispersion curves are therefore shifted to the right. Consequently, the lowest radiating space harmonic is the $m = -1$, specifically the forward $m = -1^+$ space harmonic (otherwise, in case of phase advance leftward shift, it would be the $m = 0^+$ space harmonic) since it is lowest space harmonic crossing the fast-wave region of the dispersion diagram. Due to phase reversal, the expression for the space harmonics in (2) is transformed into

$$\beta_m(\omega) = \pm \left[\beta_{TL}(\omega) + \frac{(2m+1)\pi}{p} \right], \quad m = 0, \pm 1, \pm 2, \dots \quad (3)$$

In this relation, **$\beta_{TL}(\omega)$ is the dispersion relation of the original transmission line of effective permittivity ϵ_e** , which reads

$$\beta_{TL}(\omega) = \sqrt{\epsilon_e} k_0 = \frac{\sqrt{\epsilon_e} \omega}{c}. \quad (4)$$

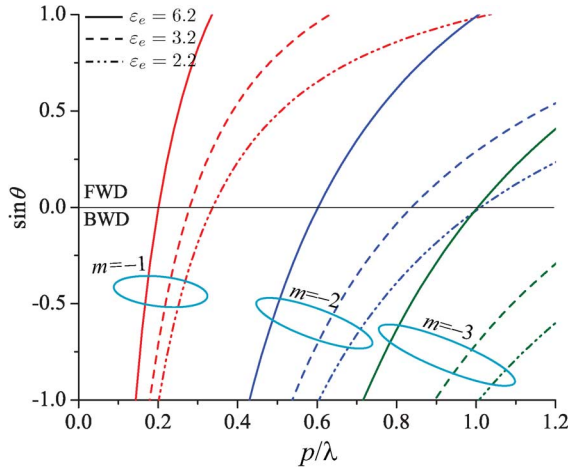


Fig. 3. Main beam angle of the first space harmonics ($m = -1, -2, -3$) versus the electrical period $p/\lambda_0 = p\omega/(2\pi c)$ (normalized frequency) for different values of ϵ_e . Single beam radiation is achieved if only one of the space harmonics is presents within the scanning range of the desired space harmonic, which is considered here to be $m = -1$.

In particular, the forward $m = -1$ space harmonic, which is the one of interest for leaky-wave radiation, is related to the transmission line dispersion relation by

$$\beta_{-1}(\omega) = \beta_{\text{TL}}(\omega) - \frac{\pi}{p}. \quad (5)$$

The angle of radiation of the beam associated with the m th space harmonic of the leaky-wave antenna is then given by the classical formula $\theta_m = \sin^{-1}(\beta_m/k_0)$, where β_m refers to the radiating space harmonic [4]. Therefore, with (3), we find that

$$\begin{aligned} \theta_m &= \sin^{-1}(\beta_m/k_0) \\ &= \sin^{-1}\left[\frac{\beta_{\text{TL}}(\omega) + (2m+1)\pi/p}{k_0}\right] \\ &= \sin^{-1}\left(\sqrt{\epsilon_e} + \frac{(2m+1)\pi c}{p\omega}\right) \\ &= \theta_m(\omega) \end{aligned} \quad (6)$$

which shows that all the space harmonics scan space as frequency is varied, despite the linearity of the dispersion curve, thanks to the $(2m+1)\pi/p$ shift in (3). Specifically, the scanning law for the $m = -1$ space harmonic reads

$$\theta_{-1}(\omega) = \sin^{-1}\left(\sqrt{\epsilon_e} - \frac{\pi c}{p\omega}\right). \quad (7)$$

The scanning angle versus frequency for the main beam of the first radiating space harmonics ($m = -1, -2, -3$), computed from (6), are plotted in Fig. 3 for different values of ϵ_e . This figure shows that several radiating beams, typically representing spurious grating lobes, may be produced at a given frequency, as a result of the penetration of several space harmonics into the fast-wave region of the dispersion diagram. The points A, B, and C in Fig. 2 indicate the backfire, endfire, and broadside radiation frequencies, respectively, of the $m = -1$ space harmonic, while point D indicates the backfire radiation frequency of the $m =$

-2 space harmonic. The $m = -1$ space harmonic below A and above B, and the $m = -2$ harmonic below D, are slow and therefore do not radiate. According to (5) or (7), the frequencies corresponding to the points A, B, and C are given by

$$f_A = f(\theta_{-1} = -90^\circ) = \frac{c}{2p(\sqrt{\epsilon_e} + 1)} \quad (8a)$$

$$f_B = f(\theta_{-1} = +90^\circ) = \frac{c}{2p(\sqrt{\epsilon_e} - 1)} \quad (8b)$$

$$f_C = f(\theta_{-1} = 0^\circ) = \frac{c}{2p\sqrt{\epsilon_e}} \quad (8c)$$

while the frequency corresponding to point D is given from (3) and (6) by

$$f_D = f(\theta_{-2} = -90^\circ) = \frac{3c}{2p(\sqrt{\epsilon_e} + 1)}. \quad (9)$$

The $m = -1$ space harmonic radiates backward (due to negative phase velocity, $v_p = \omega/\beta_{-1} < 0$) from A to C and forward (due to positive phase velocity, $v_p > 0$) from C to B, while $m = -2$ space harmonic starts to radiate at backfire at D. Therefore, $m = -1$ full-space scanning ($-90^\circ < \theta_{-1} < +90^\circ$) single beam radiation requires the satisfaction of the condition $f_D > f_B$. Using (8b) and (9), this condition translates into

$$\epsilon_e > 4. \quad (10)$$

If the effective permittivity of a transmission line does not satisfy this condition, additional periodic elements may be integrated along the structure to slow down the wave. In this manner, a new larger effective permittivity is seen by the wave (increasing the scanning sensitivity $s = d\theta/d\omega$) and (10) may be satisfied. Without phase reversal, the condition for single-beam full-space scanning [4],

$$\epsilon_e > 9 \quad (11)$$

is much more constraining, and often difficult to achieve in practice.

III. TRANSMISSION LINE MODELING

An antenna array consists of a feeding structure and several radiating elements. The proposed phase-reversal antenna (Fig. 1) may be regarded as series-fed antenna array, where the balanced transmission line sections build the series feeding structure and the cross-over conductors constitute the radiating elements. The feeding and radiating parts of the antenna are detailed in Fig. 4. Fig. 4(a) shows the line sections and their currents along the two conductors. Since the two currents flow in opposite directions, they do not contribute to radiation in the far field. Therefore, the line sections play the exclusive role of feeding structures. The radiating elements are the cross-over conductors, shown in Fig. 4(b), in between the transmission line sections. As shown in Fig. 4(c), the longitudinal (z -directed) contributions of these currents cancel out, whereas the transverse contributions added up. Assuming that the two conductors describe an angle of θ with respect to the transverse direction, the resulting effective radiating current is a purely transverse

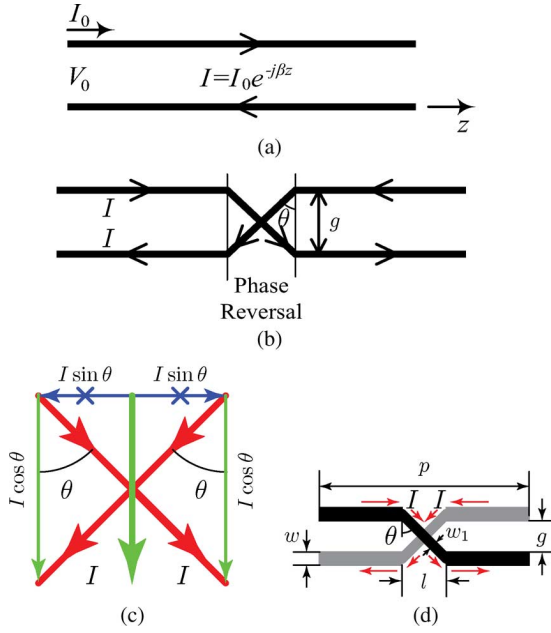


Fig. 4. Principle of feeding and radiation based on the description of the unit cell. (a) Initial balanced transmission line with its current flow. (b) Corresponding phase-reversal structure with its current distribution. (c) Effective radiating current, obtained by the vectorial summation of the cross-over currents, resulting in an equivalent vertical radiating current of magnitude $2I \cos \theta$. (d) OPS implementation of the structure with relevant parameters, the two parallel strips of the TL are shown in black and grey colors, respectively.

current with magnitude $2I \cos \theta$, where I is the magnitude of the current in each conductor.

The proposed structure may be conveniently implemented in coplanar stripline (CPS) technology. In this work, a variation of the CPS configuration is used, which is called the OPS configuration, where the two strips are placed on the two sides of a thin substrate. The resulting structure, shown in Fig. 4(d), both avoids air bridges or vias for the cross-overs and allows an easy transition from a microstrip line, while essentially retaining the fundamental features of the CPS configuration. This structure also offers a smooth phase-reversal transition with minimal discontinuity reactance and reduces the fabrication cost. Furthermore, the OPS structure with its two strips on the two layers of a thin substrate offers a large range of characteristic impedance values, where high impedance is easily achieved by increasing the offset between the two strips, while very low impedance is achieved by overlapping the two strips. This characteristic facilitates the design of the antenna and the control of its radiated power, which is particularly beneficial in nonuniform structures synthesized for optimal beam shaping.

Due to their small electrical size, the radiating currents may be modeled as infinitesimal electric dipoles with the radiation resistance [24]

$$R = 2\eta_0 \frac{2\pi}{3} \left(\frac{g}{\lambda_0} \right)^2 \quad (12)$$

where η_0 is the free-space impedance and g is the transverse length of the cross-over strips, as shown in Fig. 4(d). This formula does not account for mutual coupling between the radiators in the practical array structure. This aspect will be discussed

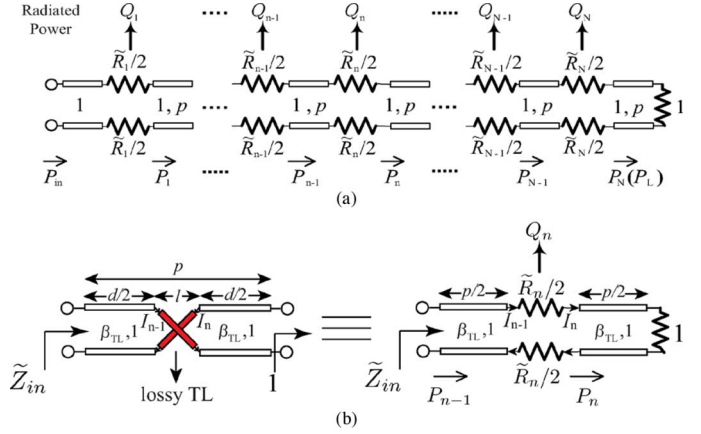


Fig. 5. Transmission line model of the phase-reversal array, where \tilde{R}_n ($n = 1, \dots, N$) is the normalized radiation resistance of the n th radiator, Q_n is the power radiated from the radiator \tilde{R}_n , and P_n is the remaining power after \tilde{R}_n . This model shows only the radiation resistances of the cross-overs and assumes ideal transmission line section interconnections. (a) Overall model. (b) Exact unit-cell structure with distributed lossy (radiating) cross-over section and equivalent lumped resistance model for the n th cell, assuming matching to the termination port Z_0 .

in Section V. In this expression, a factor of 2 is added to the conventional formula to account for the contribution of the two strip radiators. The leakage factor [4] of the antenna, α , will be proportional to this resistance distributed over the extent of the structure.

The overall N -cell leaky-wave structure can be modeled by the equivalent circuit shown in Fig. 5. In this circuit, only the radiation resistances are drawn. The reactances of the structure are omitted because they are not essential for the synthesis of the array and because they will later be absorbed in the transmission line sections.

The transmission coefficient T and reflection coefficient Γ at the n th cross-over ($n = 1, \dots, N$) can be written as a function of the normalized radiation resistance $\tilde{R}_n = R_n/Z_0$, where Z_0 is the characteristic impedance of the transmission line sections. Assuming that the $(n+1)$ th unit cell is matched to Z_0 , as will be shown in Section IV to be the case as a result of self-matching technique, Γ and T are

$$\Gamma = \frac{(\tilde{R}_n + 1) - 1}{(\tilde{R}_n + 1) + 1} = \frac{\tilde{R}_n}{2 + \tilde{R}_n} \quad (13a)$$

$$T = \sqrt{1 - \Gamma^2} = \frac{2\sqrt{1 + \tilde{R}_n^2}}{2 + \tilde{R}_n} \approx \frac{2}{2 + \tilde{R}_n} \quad (13b)$$

where the approximation holds when $R_n \ll Z_0$, i.e., $\tilde{R}_n \ll 1$. In practice, R_n is in the order of 1 to 20 Ω and Z_0 is in the order of 150–250 Ω so that \tilde{R}_n is in the order of 0.005–0.1, which largely justifies the approximation. The corresponding reflections range from -20 to -40 dB, as confirmed in Fig. 6(a). Though the reflection for a single unit is small, as the number of unit cells increases, the total reflection at the input of the antenna increases at the broadside frequency, where the phase delay of the interconnecting transmission lines is π . Suppose the traveling-wave antenna has $N = 40$ unit cells along the transmission line, the total reflection coefficient at the input port

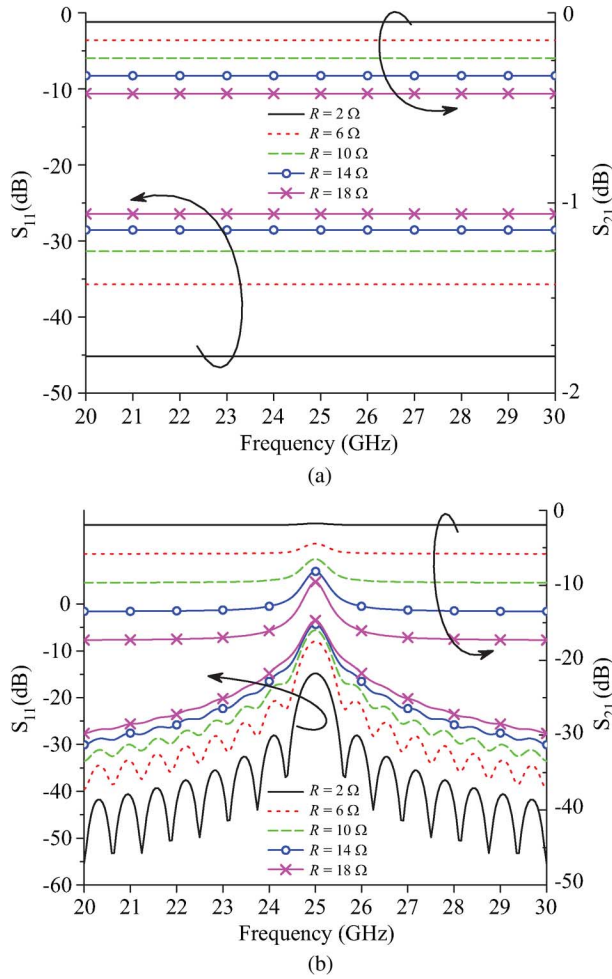


Fig. 6. S -parameters: (a) for a one-cell phase-reversal antenna and (b) for a 40-cell phase-reversal antenna simulated from the equivalent transmission line model of Fig. 5 *without any unit-cell matching*. The radiation resistance R varies in the range from 2 to 18 Ω , which covers the typically required radiation resistances of a traveling-wave antenna. The load and source impedances are of $Z_0 = 180 \Omega$. The length of the transmission line sections between neighboring unit cells are of 180° at the center frequency 25 GHz.

is shown in Fig. 6(b). As the radiation resistance increases from 2 to 18 Ω , the return loss at this frequency decrease from 15 to 4 dB and the insertion loss show a dip. This means that the radiated power drops quickly at this frequency. In contrast, away from this frequency, good impedance matching is maintained because the reflections from the large number of unit cells tend to cancel each other for other than π phase shifts.

This phenomenon can also be explained from the dispersion diagram of the periodic structure, which is plotted in Fig. 7 for the case of a uniform array ($R_n = R = \text{const.}$, $n = 1, 2, \dots, N$) using the circuit model of Fig. 5. A sharp drop of the leakage factor α occurs near the broadside ($\beta = 0$) frequency, where the electric length of the unit cell equals π . This point corresponds to a stopband, which opens up in the presence of a periodic discontinuity. In this structure, as mentioned previously, the discontinuity is small, and this is the reason why the stopband is not very wide. Note that in the same frequency region, the phase constant β also displays a very small variation where it becomes slightly nonlinear, as a consequence of the small couplings between oppositely directed space har-

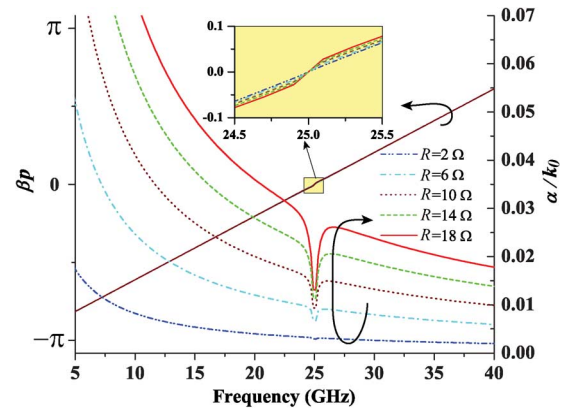


Fig. 7. Dispersion diagrams for the periodic (infinite) antenna structure computed from the circuit model of Fig. 5 with the parameters $\beta p = \pi$ at 25 GHz, $Z_0 = 165 \Omega$ for several values of the radiation resistances R . (The structure is uniform, i.e., $R_n = R$, $n = 1, 2, \dots$)

monics. This result shows that, independent of the possible reactance discontinuities (not considered yet), small resistance discontinuities produce a stopband, where α drops toward zero at $\beta = 0$, which prevents efficient broadside radiation [18]. In fact, the reactive discontinuities of the structure will next be used to achieve a near-perfect matching of the unit-cell so as to completely close the stopband and thereby achieve efficient broadside radiation.

For the synthesis of the array, which consists of determining the proper values of the set of resistors \tilde{R}_n and which will be presented in Section V, a proper relation must be established between the power entering the n th unit cell, P_{n-1} , and the power radiated by this cell, Q_n , i.e., we need to determine Q_n/P_{n-1} . Referring to Fig. 5(b), the impedance seen at the input of the n th unit cell, assuming that this cell is matched to Z_0 (as will be ensured later) is

$$\tilde{Z}_{\text{in}} = 1 + \tilde{R}_n. \quad (14)$$

The radiation power Q_n is due to the radiation related to \tilde{R}_n , while the power P_{n-1} will be radiated partly by \tilde{R}_n and partly by the rest of the structure, which is represented by the matched resistance Z_0 in Fig. 5(b). Consequently,

$$\frac{Q_n}{P_{n-1}} = \frac{\tilde{R}_n}{\tilde{R}_n + 1}. \quad (15)$$

IV. SUPPRESSION OF THE OPEN STOPBAND FOR BROADSIDE RADIATION

The results shown in Fig. 6 show that the proposed periodic phase-reversal antenna cannot radiate efficiently at broadside with radiation resistances only due to the presence of an open stopband. This section will show that addition of proper reactance providing matching of the unit cell leads to complete closure of this stopband, and subsequently, to efficient broadside radiation.

A. Unit Cell Impedance Matching

A structure composed of N unit cells will automatically be matched if all the unit cells are matched, while a very small

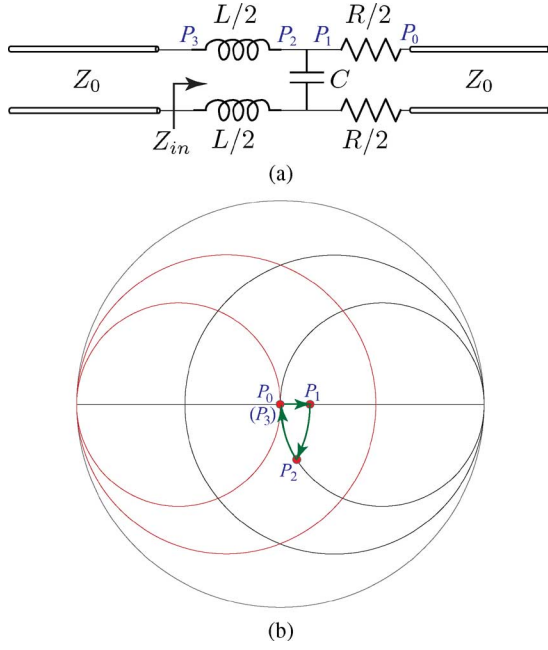


Fig. 8. Principle of unit-cell matching. (a) Equivalent circuit. (b) Smith chart trajectory along the points P_0 to P_3 indicated in (a).

mismatch in the unit cell will be magnified by the factor N in the response of the overall structure. Therefore, let us derive now the condition for matching of the unit cell. This is best accomplished with the help of the circuit model shown in Fig. 8(a), where the structure is assumed to be perfectly matched to a port impedance of Z_0 . The impedance to the right at this input of the unit cell is

$$Z_{in} = j\omega L + \frac{1}{j\omega C + \frac{1}{Z_0 + R}}. \quad (16)$$

This impedance must be equal to the impedance Z_0 seen to the left for matching. This condition yields, after equating the real and imaginary parts of the relation $Z_{in} = Z_0$,

$$L = \frac{\sqrt{Z_0 R}}{\omega} = \frac{Z_0 \sqrt{\tilde{R}}}{\omega} \quad (17a)$$

$$C = \frac{\sqrt{Z_0 R}}{\omega Z_0 (Z_0 + R)} = \frac{\sqrt{\tilde{R}}}{\omega Z_0 (1 + \tilde{R})}. \quad (17b)$$

The impedance-matching procedure following this pair of relations is illustrated by the trajectory drawn in the Smith chart of Fig. 8(b). Since the normalized resistance \tilde{R} , representing the radiation of a single cross-over, is very small in practice, the point P_1 is very close to the point P_0 . Therefore, only the required values for L and C are very small, and hence, easy to achieve.

The dispersion diagram for the circuit of Fig. 8(a) (including the matching reactance L and C) is shown in Fig. 9. The phase constant β and leakage factor α are unaltered compared to the case of Fig. 7 (without the matching reactance) at frequencies away from broadside. In contrast, the abrupt broadside variations observed in Fig. 7 and corresponding to the mismatch shown in Fig. 6(b) have been almost completely suppressed as a result of matching. In particular, the leaky-wave factor does not

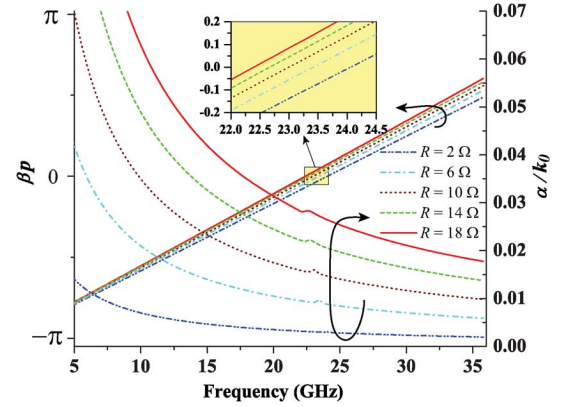


Fig. 9. Dispersion diagram for the periodic (infinite) antenna structure computed from the unit-cell matching circuit of Fig. 8(a) with the same parameters as in Fig. 7 and for several different values of the radiation resistances R . The LC values used are computed from R by (17a) and (17b).

drop significantly, which indicates a nearly complete suppression of the open stopband and guarantees a continuous scanning through broadside with an almost constant radiation efficiency, as will be demonstrated experimentally in Section VI. It should also be noted that increasing the radiation resistance not only increases the leakage factor, but also slightly increases the phase constant, as may be easily verified by computing the second-order approximation phase constant of a lossy transmission line.

The corresponding matching benefits are seen in Fig. 10(a) and (b). Excellent impedance matching is achieved at all the frequencies, with the lowest return loss at the broadside frequency, where matching was specifically performed. The insertion loss of the corresponding two-port structures is almost constant with frequency, which implies a constant radiation efficiency.

Another possible matching technique is shown in Fig. 11. This technique uses antiparallel stubs placed at the center of the transmission line sections. In this configuration, the stubs do not radiate, due to their antiparallel current contributions, and they are thus used exclusively for matching. The small reflections induced from these discontinuities are cancelled out with the reflections from the crossover discontinuities since the distance between them is of $\lambda_g/4$ at broadside frequency. This approach represents an alternative design technique, which may be used to relax the constraints on the radiating cross-overs in some specific applications.

B. Implementation and Results

As previously mentioned, the natural reactance discontinuities existing in the practical implementation of the phase-reversal structure in addition to those due to the radiation resistances may be used for the matching procedure just described. Fig. 12 shows the structure proposed for cross-over self-matching, along with the corresponding local characteristic impedance. The impedance steps at the edges of the cross-over are due to the stepped-impedance discontinuities between the low-impedance interconnecting transmission lines and the higher impedance cross-overs, which can be modeled by lumped series inductances [25]. Across the cross-over region,

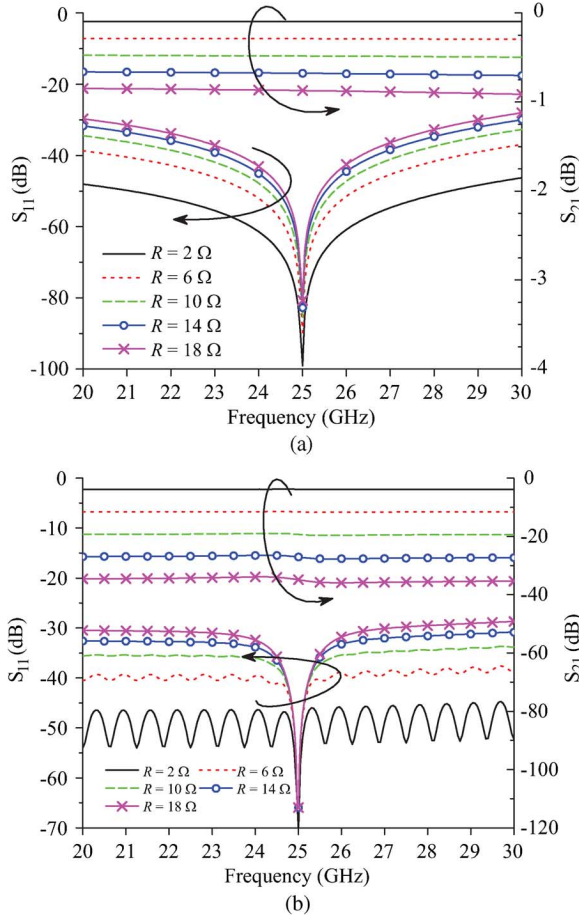


Fig. 10. S -parameters: (a) for a one-cell phase-reversal antenna and (b) for a 40-cell phase-reversal antenna simulated from the equivalent transmission line model of Fig. 5, as in Fig. 6, but with the LCR unit-cell matching depicted in Fig. 8.

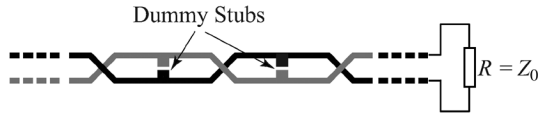


Fig. 11. Phase-reversal antenna structure using dummy stubs to suppress the open stopband.

the impedance experiences a decrease followed by an increase, due to the capacitive loading effect of the strip overlapping region. The equivalent circuit of Fig. 8(a) provides a qualitative idea of the proposed self-matching technique. However, its parameters are practically difficult to extract, except for the radiation resistance, which can be estimated by commercial software such as IE3D or the High Frequency Structure Simulator (HFSS). Therefore, the overall cross-over structure is simply designed and optimized by full-wave analysis in practice. This approach also ensures proper account of the effects of mutual coupling between the unit cell. Matching optimization involves tuning of the parameters w_1 , l , and w_2 defined in Fig. 12.

Fig. 13 plots the phase constant β and leakage factor α of the periodic phase-reversal structure extracted from full-wave simulation [26], [27], for different number N of unit cells (1–7).

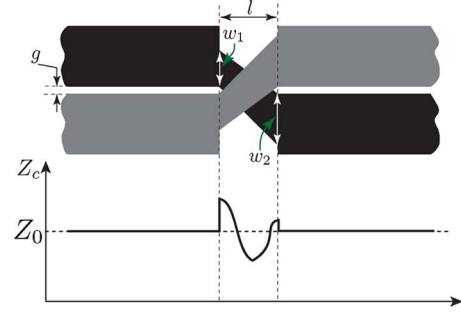


Fig. 12. Matched unit-cell cross-over structure and qualitative local characteristic impedance. The impedance just below the overlapping region of the two strips is decreased due to capacitive coupling.

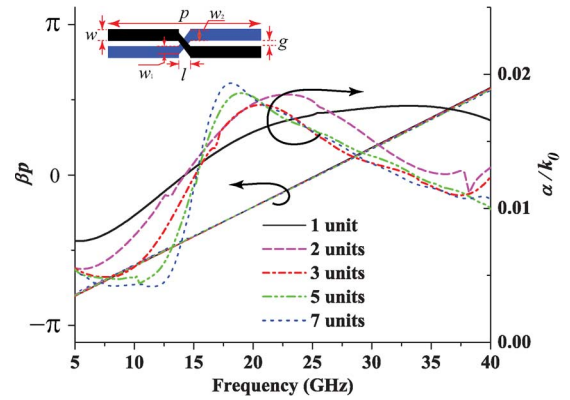


Fig. 13. Complex propagation constant ($\gamma = \alpha + j\beta$) of the matched (Fig. 12) phase-reversal antenna computed by full-wave analysis (method of moments (MoM) IE3D) and then applying Bloch-wave analysis for the parameters $\epsilon_r = 2.94$, $p = 4.1$ mm, $g = 0.2$ mm, $l = 0.15$ mm, $w = 0.3$ mm, $w_1 = 0.2$ mm, and $w_2 = 0.3$ mm. The number of unit-cells varies from 1 to 7. The extracted leakage factor converged after five units.

While β is stable versus N , α only converges for $N > 3$. This N dependence of α is due to the mutual coupling existing between the unit cells. The normalized leakage factor (α/k_0) varies approximately from 0.01 to 0.02 above 16 GHz, which corresponds to the border frequency of the radiation cone represented in Fig. 2. Below 16 GHz, α sharply drops to a value close to zero due to the absence of radiation. Above 16 GHz, in the radiation zone, β varies linearly with frequency across broadside and α does not experience any significant drop; α/k_0 decreases linearly with frequency and is smooth near broadside. A linearly decreasing α/k_0 indicates a constant leakage (α) over frequency, giving rise to a perfectly equalized radiation efficiency. Since the antenna becomes electrically larger as frequency increases, the correspondingly increasing directivity is naturally expected to result in increasing gain.

V. ARRAY SYNTHESIS

A. Synthesis of the Radiation Resistance

The procedure of synthesizing the attenuation constant (α) of a leaky-wave antennas is well illustrated in [28]. For the proposed phase-reversal antenna, the array synthesis problem consists in determining the resistances \hat{R}_n ($n = 1, \dots, N$) of the structure for a given desired radiation efficiency η and given desired radiation aperture $Q(z)$, which is approximated by distri-

bution of radiated powers Q_n ($n = 1, \dots, N$). Thus, we are seeking an expression for \tilde{R}_n as a function of η and Q_n .

The available powers before and after the cross-over resistance \tilde{R}_n , which are denoted P_{n-1} and P_n , respectively, in Fig. 5, are found to be

$$P_{n-1} = I_{n-1}^2(\tilde{R}_n + 1) \approx I_n^2(\tilde{R}_n + 1) \quad (18)$$

$$P_n = I_n^2 \cdot 1 \quad (19)$$

where the approximation in (18) is justified by the small amount of radiation leakage ($\tilde{R}_n \ll 1$) loss occurring in the cross-over sections. The resistance \tilde{R}_n may be then written as

$$\tilde{R}_n = \frac{P_{n-1} - P_n}{P_n} = \frac{Q_n}{P_n} \quad (20)$$

where P_n is the sum of the powers Q_m radiated by the next elements ($m = n + 1, \dots, N$) and of the power consumed in the load, P_L , i.e.,

$$P_n = \sum_{m=n+1}^N Q_m s^{n-m} + P_L s^{n-N}. \quad (21)$$

In this relation, $s = e^{-2\alpha_{TL}P}$, where α_{TL} is the attenuation factor of the transmission lines, which reduces to unity in the limiting case of lossless lines. Combining (20) and (21) yields

$$\tilde{R}_n = \frac{Q_n}{\sum_{m=n+1}^N Q_m s^{n-m} + P_L s^{n-N}}. \quad (22)$$

The radiation efficiency of the antenna is

$$\eta = \frac{\sum_{n=1}^N Q_n}{P_{in}} \approx \frac{P_{in} - P_L}{P_{in}} \quad (23)$$

where the approximation transforms into an equality as $\alpha_{TL} \rightarrow 0$ and where the input power P_{in} reads

$$P_{in} = \sum_{n=1}^N Q_n s^{1-n} + P_L s^{1-N}. \quad (24)$$

Inserting (24) into (23), and next substituting the resulting expression for P_L into (22) leads to the sought synthesis result

$$\tilde{R}_n = \frac{Q_n/s^n}{\eta^{-1} \sum_{m=1}^N \frac{Q_m}{s^m} - \sum_{m=1}^n \frac{Q_m}{s^m}} \quad (25)$$

which reduces to

$$\tilde{R}_n = \frac{Q_n}{\eta^{-1} \sum_{m=1}^N Q_m - \sum_{m=1}^n Q_m} \quad (26)$$

in the case of transmission lines with negligible loss ($\alpha_{TL} \approx 0$). Naturally, the achievable set of resistances will be limited by technological constraints, in particular by the achievable range of sizes of the cross-over sections, which sets limitations to the possible designs.

B. Cross-Over Realization of the Radiation Resistance

The geometric parameters of the cross-overs (Fig. 12) required to implement the radiation resistances prescribed by (26)

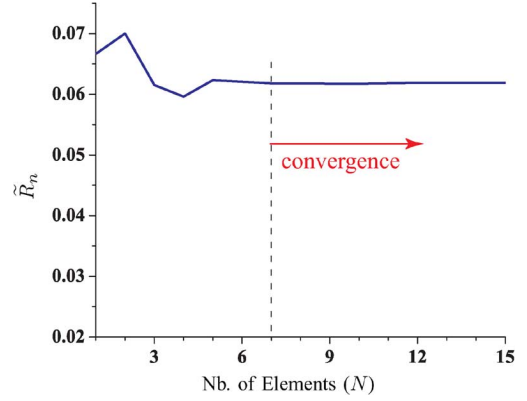


Fig. 14. Radiation resistance R extracted by (29) for a uniform ($R_n = R = \text{const.}$) phase-reversal antenna with different number of elements $N = 1, \dots, 15$. The resistance value converges, indicating suppression of the edge effects, after seven elements.

are determined by full-wave simulation or measurement. Equation (12) may be used as a first guess for the layout of the cross-overs. The design is next performed by iterative full-wave analysis via the scattering parameters. In order to account for mutual coupling between the unit cells, an N -cell uniform ($R_n = R = \text{const.}$) antenna structure terminated the end by a matched load is analyzed, where N is made large enough to ensure convergence of the results, interpreted as the suppression by dilution of the edge effects of the structure. It is assumed that the effects of mutual coupling of nonuniform antenna designs will not depart significantly from those of the uniform extraction model.

Since the unit cells are assumed to be well matched, the ratio of the input to the load powers may be obtained by writing the ratio of (19) to (18), $P_n/P_{n-1} = 1/(\tilde{R}_n + 1)$ for $n = N$ to $n = 1$, and taking the product of all the resulting expressions, which yields

$$\frac{P_L}{P_{in}} = 1/(\tilde{R}_n + 1)^N. \quad (27)$$

From the viewpoint of the scattering parameters, this ratio may also be written

$$\frac{P_L}{P_{in}} = \frac{|S_{21}|^2}{1 - |S_{11}|^2}. \quad (28)$$

The resistance \tilde{R}_n is then obtained by equating these ratios

$$\tilde{R}_n = \left(\frac{1 - |S_{11}|^2}{|S_{21}|^2} \right)^{\frac{1}{N}} - 1. \quad (29)$$

Fig. 14 plots the radiation resistance extracted from (29) for a uniform ($R_n = R = \text{const.}$) phase-reversal antenna with a different number of elements N . Since this procedure is fulfilled by analyzing the antenna as a truncated structure, the extracted radiation resistance only converges after exceeding certain number of cells [29]. As shown in Fig. 14, convergence to the final value of the resistance, taking into account the effects of mutual coupling in a practical structure, is achieved after seven unit cells. Below this number, the dissymmetry of the coupling distribution due to the finiteness of the structure affects the coupling results. Beyond this number, this effect is diluted across

the structure since the ratio of the number of ports (i.e., two) over the number of coupled cells, becomes negligible. Note that this extraction technique includes tuning of the different geometrical parameters to maintain the matching of the unit cell. The technique provides a fairly accurate model of the unit cell as a basis for the synthesis of the complete N -cell structure, which then requires only minor fine-tuning.

C. Antenna Design Procedure

The proposed phase-reversal antenna is characterized by the following parameters: frequency range of operation, scanning angle θ , 3-dB beamwidth $\Delta\theta_{3\text{ dB}}$ (directivity), radiation efficiency η , and sidelobe level (SLL). Based on the specifications for these parameters, the design procedure may be articulated as follows.

- 1) Since all the above parameters change with scanning, the design must be performed at a selected angle of radiation. The best approach is to choose the angle located at the middle of the scanning angular range so as to minimize the departure from the specifications as scanning occurs. In typical applications, this angle will be the broadside angle, corresponding to a symmetric scan around the broadside.
- 2) Determine the aperture distribution $Q(z)$ (e.g., uniform, Taylor, binomial, etc.) required for the specified value of SLL.
- 3) Determine, for the chosen substrate (and its effective permittivity ϵ_e), the period p of the structure corresponding to the specified frequency range (Fig. 2).
- 4) Determine the number of unit cells N , corresponding to the length $(N-1)p$, providing the specified value of $\Delta\theta_{3\text{ dB}}$ for the distribution determined at 2); this, with 2), yields the local radiated powers Q_n for $n = 1, \dots, N$.
- 5) Compute the values of \tilde{R}_n for $n = 1, \dots, N$ using (26) for the specified value of η .
- 6) Synthesize (typically by full-wave simulation) the corresponding cross-over geometrical parameters, which are essentially $w_n(\tilde{R}_n)$ and $g_n(\tilde{R}_n)$; this requires some minor matching adjustments.
- 7) Simulate and optimize the overall antenna.

D. Example: Uniform-Aperture Antenna

As an example, let us design a phase-reversal antenna with the following specifications: center frequency of 25 GHz, symmetric scanning range around broadside, a 3-dB beamwidth of 4° , a radiation efficiency of 80%, and an SLL of at least 13 dB. Following the above design procedure, we have the following.

- 1) Since a symmetric scanning range around broadside is required, the angle of design will be chosen as $\theta = 0^\circ$.
- 2) A uniform aperture, characterized by $\text{SLL} = 13.3\text{ dB}$ [24] is sufficient to meet the SLL specification. Thus, $Q(z) = Q_0 = \text{const.}$ over the antenna structure.
- 3) The specified frequency corresponds to the dispersion diagram of Fig. 2, which uses a substrate of $\epsilon_e = 2.2$, leading to a period of $p = 4.1\text{ mm}$.
- 4) According to the corresponding array factor, $N = 41$ unit cells are required to provide $\Delta\theta_{3\text{ dB}} = 4^\circ$; correspondingly, $Q_1 = Q_2 = \dots = Q_N = Q_0$ for $n = 1, \dots, N$.

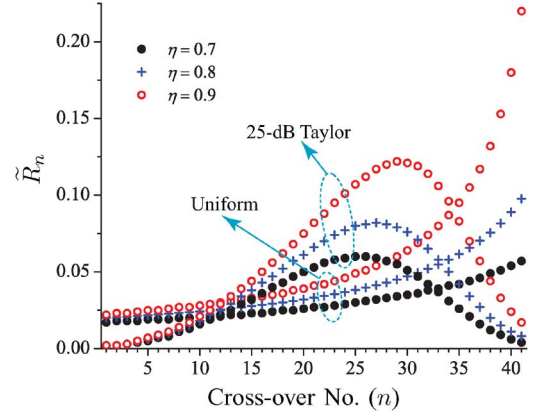


Fig. 15. Distribution of the normalized radiation resistances for a 41-cell phase-reversal antenna for the efficiencies of 70%, 80%, and 90%. The synthesized resistances for both the uniform distribution (maximum directivity) and the Taylor distribution with $\text{SLL} = 25\text{ dB}$ (reduced SLL) are shown.

- 5) For constant $Q_n m$, (26) reduces to

$$\tilde{R}_n = \frac{\eta}{N - \eta n} = \frac{0.8}{41 - 0.8n}. \quad (30)$$

We see that \tilde{R}_n decreases as n increases, i.e., as one moves from the source to the load, for a uniform aperture. This is because the fraction of power radiated in each unit cell ($\propto \tilde{R}_n$), to be constant in absolute terms ($Q_n = \text{const.}$), must compensate for the decay of the available power (P_n) [see (20)]. This resistance distribution is plotted in Fig. 15, which also shows the cases of $\eta = 70\%$ and $\eta = 90\%$, as well as the case of a Taylor aperture [24], for comparison. This graph shows that, for a given antenna length or directivity, the range of radiation resistances is proportional to the radiation efficiency. This is because a higher efficiency requires a larger amount of radiation per unit length to reduce the amount of power wasted in the load. When the required efficiency exceeds a given limit (e.g., around 90% here), the extreme (most radiating) phase-reversal element become very difficult to realize due to the too large required radiation resistances.

- 6) In order to follow the requirement of increasing resistances along the structure, the width and length of the cross-overs must be increased along the antenna, while the characteristic impedance of the interconnecting transmission line sections must be kept constant to avoid mismatch. This leads to a tapered structure, as shown in Fig. 16. In this structure, the gap between the strips (g) of the transmission line sections are progressively increased to achieve increasing radiation resistances, while the width (w) of the lines is also increased to maintain a constant characteristic impedance. To ease the tedious process of full-wave simulating, all of 41 unit cells of the antenna, an interpolation technique, limiting here the number of simulated cells to seven, is used. First, the strip widths w are synthesized for the required (constant) characteristic impedance (Z_0). Second, after designing proper self-matching cross-overs following the technique described in Section III, the corresponding radiation resistances (\tilde{R}_n) are extracted. Finally,

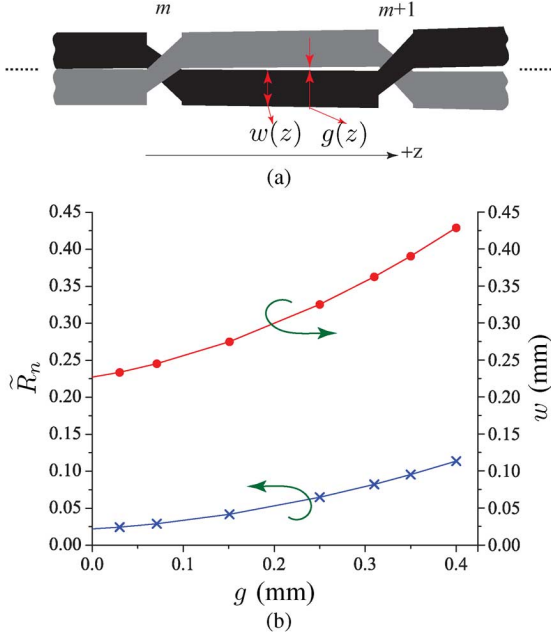


Fig. 16. Unit cell design for the phase-reversal antenna tapered so as to produce a uniform effective aperture (broadside case). This figure may be used for design in connection with the synthesis results of Fig. 15. (a) Continuously tapered unit cell. (b) Nonuniform strip with w and resistance \tilde{R}_n distributions versus the gapwidth g required to maintain a constant characteristic impedance of $Z_0 = 165 \Omega$. The results are for a 20-mil Roger 6002 substrate and radiation efficiency $\eta = 80\%$.

as shown in Fig. 16(b), a second-order curve-fitting technique is utilized to interpolate the functions $w(n)$ and $g(n)$

$$\tilde{R}_n = a_0 + a_1g + a_2g^2 \quad (31a)$$

$$w = b_0 + b_1g + b_2g^2 \quad (31b)$$

where $a_0 = 0.0218$, $a_1 = 0.07372$, $a_2 = 0.39004$; $b_0 = 0.22675$, $b_1 = 0.20813$, and $b_2 = 0.74426$, and where g is in millimeters. With this interpolation, only a reduced number of unit cells must be synthesized.

The above design has assumed a perfectly flat phase distribution across the antenna structure at broadside. However, in practice, the tapering required for a nonuniform resistance distribution also affects the phase distribution since larger resistors require longer strips [see (12)] and larger values of L and C for self-matching, which exhibit larger phase delays. In a uniform aperture antenna, this will cause the phase to increase along the structure. Fig. 17 shows the phase-error distribution related to this effect. Fig. 17(a) shows phase error occurring in each unit cell with respect to the phase shift across the first cell, and the corresponding radiated power ratio Q_n/P_n , showing that the phase error is inversely proportional to the radiated power ratio. The phase errors accumulate along the structure and produce the phase distribution shown by the circle curve in Fig. 17(b). In the graph, this curve is fitted by a third-order Taylor approximation, and the corresponding linear, quadratic, and cubic terms are shown separately. According to array theory [24], a linear phase error distribution tends to slightly tilt the main beam by a certain angle. Here, the tilt will be in the forward direction due

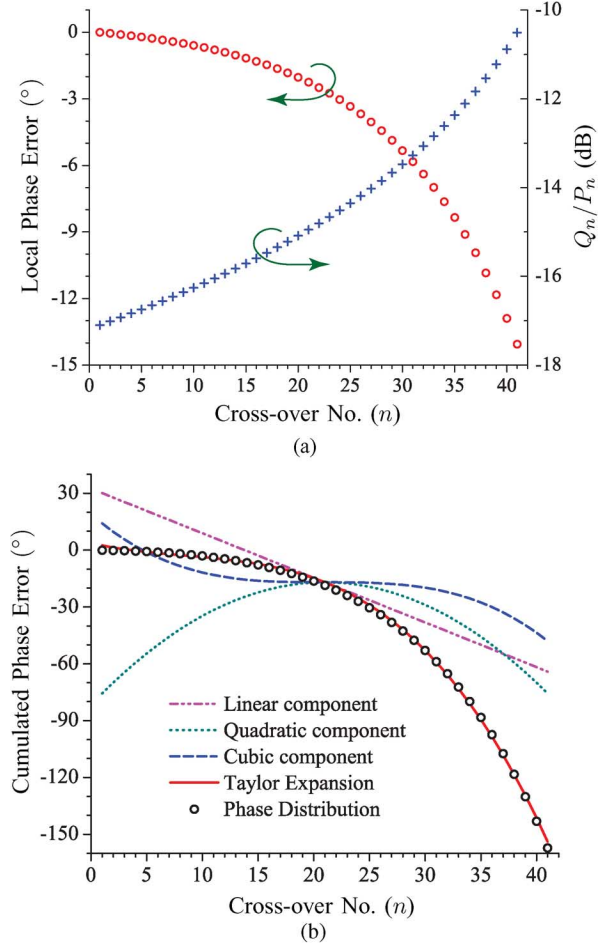


Fig. 17. Phase error distribution (at broadside) along a 41-cell uniform-aperture phase-reversal antenna (broadside case) obtained by full-wave simulation. (a) Local error (phase shift across the n th minus phase shift across the first), and corresponding radiated power ratio Q_n/P_n . (b) Cumulated error, with corresponding Taylor expansion fitting: linear, quadratic, and cubic.

to the increasing delay and the broadside frequency will therefore be shifted to a lower value. The quadratic error term primarily reduces the directivity and symmetrically degrades the SLL, while it leaves symmetric radiation patterns unaffected. The cubic error term introduces asymmetrical shoulders around the main lobe.

The SLL of the uniform-aperture antenna (-13.3 dB) can be decreased by using a Taylor aperture distribution [24]. Fig. 15 also shows the radiation resistance distribution for a 41-element phase-reversal antenna with 25-dB SLL. The upper limit of the resistance range is close to that of the uniform case. In contrast, the lower limit is much lower and close to zero, which can be implemented with very short and strongly overlapping (nonradiating transmission line like region) cross-overs.

VI. EXPERIMENTAL DEMONSTRATION

A. Antenna Design

The overall antenna is designed on a Roger 6002 substrate with a height of 20 mil and permittivity of 2.94. It is simulated with IE3D (MoM) as a two-port structure. The simulation ports are set to 165Ω , corresponding to the characteristic

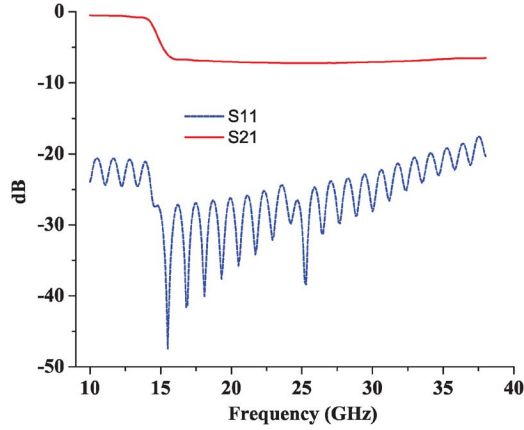


Fig. 18. Simulated (IE3D MoM) S -parameters for the phase-reversal antenna without input impedance transformer for the geometrical parameters found from Fig. 16(b).

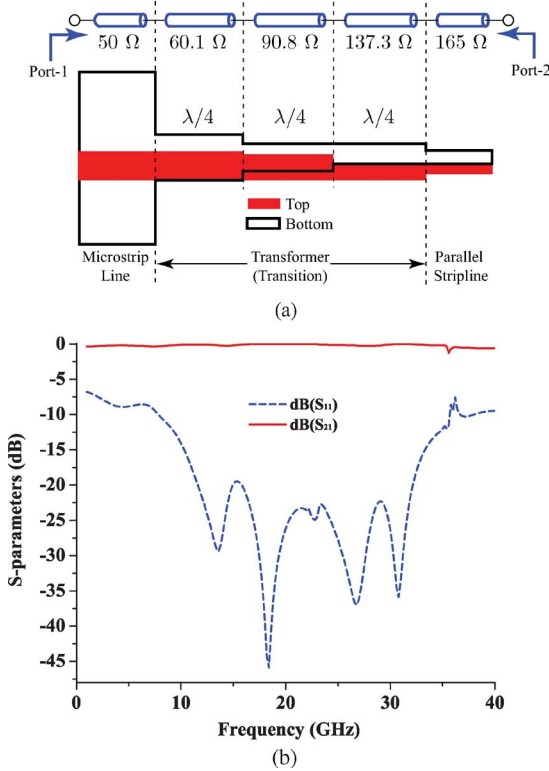


Fig. 19. Three-stage balun and impedance-transformer transition used the excite the phase-reversal antenna. (a) Structure layout and parameters. (b) Simulated S -parameters.

impedance of the transmission lines sections between the cross-overs. Fig. 18 shows the simulated S -parameters. Perfect impedance matching is observed, validating the proposed unit-cell matching technique, with a return loss higher than 25 dB at the broadside-radiation frequency, 25 GHz. Thanks to unit-cell matching, the open stopband is completely suppressed. The insertion loss is almost perfectly flat, at a value of around -7.6 dB corresponding to 83% radiation efficiency (very close to the targeted 80% efficiency), immediately after penetration of the $n = -1$ space harmonic into the fast-wave region of the dispersion diagram, at 16 GHz (Fig. 2).

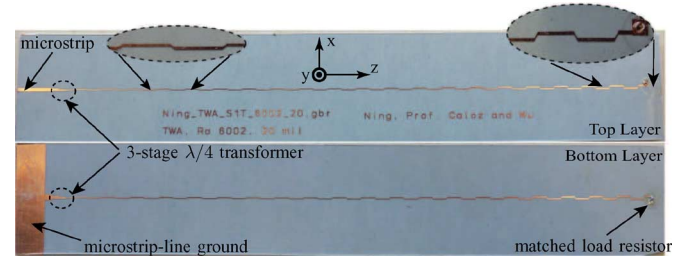


Fig. 20. Phase-reversal antenna prototype.

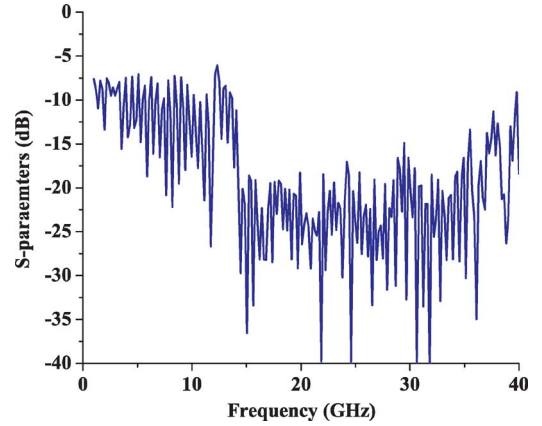


Fig. 21. Measured return loss for the traveling-wave antenna of Fig. 20.

B. Design of Input Balun and Impedance-Transformer Transition

The antenna will be terminated by a matched chip resistor. In contrast, a proper feeding mechanism is required at the input. Since the antenna is balanced and the measurement instrumentation is unbalanced, a balun is required at both ends of the structure. Moreover, impedance transformation from the 165- Ω impedance of the antenna to 50 Ω of the instruments. A three-stage balun and impedance-transformer transition is used for this twofold purpose. Fig. 19(a) shows the transmission line model and layout of the transition. A 50- Ω microstrip line is followed by three sections of high-impedance parallel-strip line sections with the same length of $\lambda/4$ at the center frequency (broadside-radiating frequency). To achieve good matching over the entire scanning bandwidth, an in-band equal-ripple Chebyshev design is performed [30], using the characteristic impedances of $Z_{01} = 60.1$ Ω , $Z_{02} = 90.8$ Ω , and $Z_{03} = 137.3$ Ω for the three different sections. The simulated S -parameters of the transition is shown in Fig. 19(b). The resulting return loss exceeds 20 dB from 11 to 33 GHz.

C. Prototype

The overall fabricated antenna, including the leaky-wave structure and the input transition, is shown in Fig. 20. A 180- Ω thick-film surface-mount flip-chip resistor (RCD-0302PW1800L) from IMS Inc., Portsmouth, RI, is connected across the parallel-strip line through a vertical via at the end to terminate and match the antenna. The resistance value of the load differs by 15 Ω from the desired 165 Ω and the vias creates additional undesired reactance load, but these imperfections only produce minor reflections at the end. The overall 41-cell

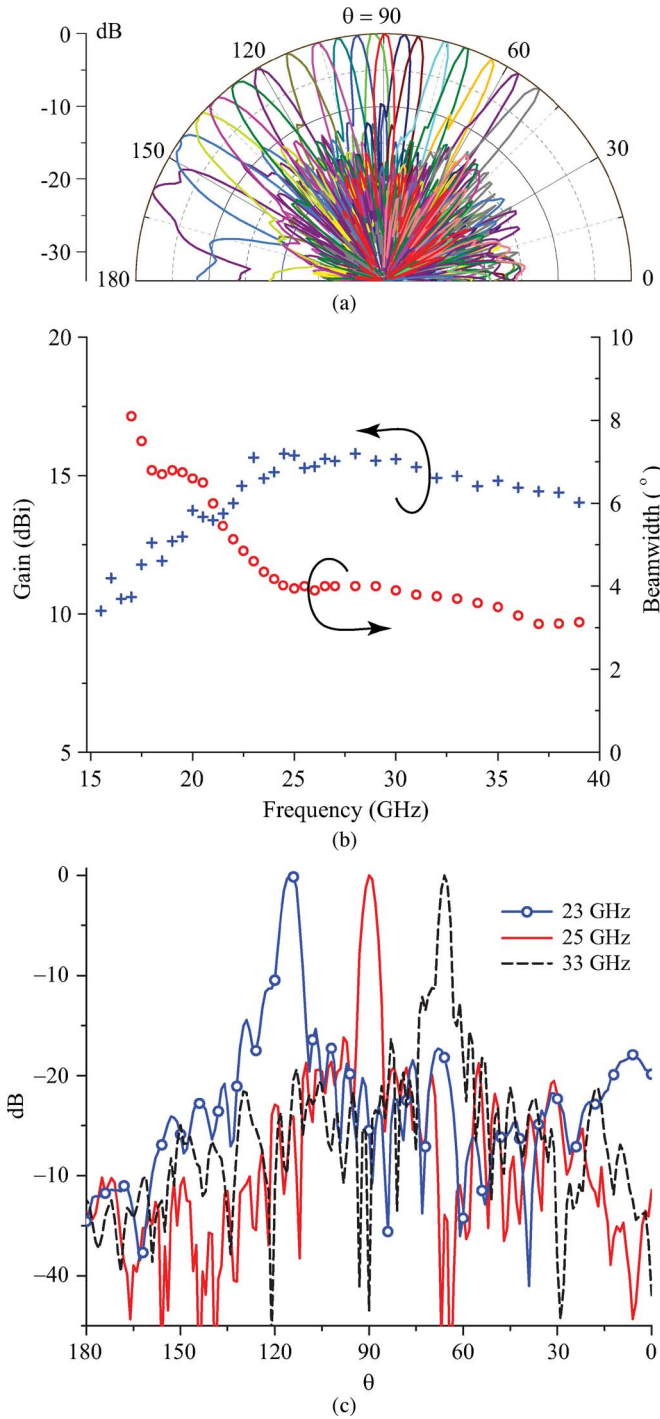


Fig. 22. Measured radiation performance (E_ϕ) in H -plane (yz -plane) for the phase-reversal antenna of Fig. 20. (a) Scanned radiation patterns at the frequencies 16, 16.5, 17, 17.5, 18, 19.5, 20.5, 21.5, 22.5, 23.5, 24.5, 25, 27, 29, 31, 33, 35, 37, and 39 GHz. Broadside radiation occurs at 25 GHz. (b) Gain and beamwidth versus frequency. (c) Rectangular plot of the radiation pattern at 23, 25 and 33 GHz, which corresponds to the main beam angle at $\theta = 115^\circ$, $\theta = 90^\circ$ (broadside), and $\theta = 66^\circ$.

antenna including the transitions and connection microstrip line is about 180-mm long.

D. Results

The antenna follows the design of Section V. Fig. 21 shows the measured S_{11} of the prototype. The filtering effect of the

three-stage Chebyshev transition circuit reduces the return loss by around 10 dB at the upper edge of the leaky-wave radiation band.

Fig. 22(a) shows the measured co-polarized (E_ϕ) radiation patterns of the antenna in the H -plane (yz -plane) for a frequency sweep from 16 to 39 GHz. Fig. 22(b) shows the corresponding measured gain and beamwidth. Broadside radiation occurs at 25 GHz. At this point, the measured gain is of 15.7 dBi and the measured 3-dB beamwidth is of 4° . The beamwidth slowly decreases as frequency increases since the antenna aperture increases as the wavelength decreases. However, the beamwidth next saturates and eventually increases as the beam angle approaches endfire, where the effective antenna aperture is reduced. The SLL of the radiation pattern in the plane of beam scanning is of -16.2 dB at broadside frequency, which is 3 dB lower than the expected for an antenna with an exact uniform aperture distribution. The reason for this discrepancy may be the differences due to the curve-fitting design technique used in (31). To better evaluate the results, a rectangular plot of three radiation patterns at 23, 25, and 33 GHz are shown in Fig. 22(c). As expected from the cubic term of the phase-error distribution, the main lobe exhibits a shoulder at certain frequencies. Some of the spurious sidelobes (below -15 dB) are due to re-radiation from the signal reflected from the end chip resistor at mirrored angles with respect to broadside.

VII. CONCLUSION

A novel full-space scanning periodic phase-reversal leaky-wave antenna array, radiating in the $m = -1$ space harmonic, has been proposed, designed in OPS technology, implemented, and measured. In contrast to previously reported antennas of this type, this antenna radiates from its phase-reversing sections as opposed to from the interconnecting transmission line sections or the stubs, which allows for small leakage factor and subsequently large directivities. As a result of phase reversal, single-beam full-space scanning can be achieved on a relatively low-permittivity substrate. The open stopband, which typically plagues broadside radiation in periodic leaky-wave antennas, is completely suppressed thanks to a special unit-cell matching technique. A millimeter-wave leaky-wave antenna with uniform aperture distribution has been designed using an efficient synthesis procedure. Continuous single-beam full-space frequency scanning has been demonstrated experimentally for this antenna. The measured beamwidth and gain at the broadside frequency of 25 GHz are of 4° and 15.7 dBi, respectively.

REFERENCES

- [1] R. E. Collin and R. F. Zucker, Eds., *Antenna Theory, Part II*. New York: McGraw-Hill, 1969.
- [2] C. A. Balanis, *Antenna Theory: Analysis and Design*, 2nd ed. New York: Peregrinus, 1996.
- [3] F. J. Zucker, "Surface-wave antennas," in *Antenna Engineering Handbook*, J. Volakis, Ed., 4th ed. New York: McGraw-Hill, 2007, ch. 11.
- [4] A. A. Oliner and D. R. Jackson, "Leaky-wave antennas," in *Antenna Engineering Handbook*, J. Volakis, Ed., 4th ed. New York: McGraw-Hill, 2007, ch. 10.
- [5] R. S. Elliott, *Antenna Theory and Design*. New York: Prentice-Hall, 1981.

- [6] M. Takahashi, J. Takada, M. Ando, and N. Goto, "A slot design for uniform aperture field distribution in single-layered radial line slot antennas," *IEEE Trans. Antennas Propag.*, vol. 39, no. 7, pp. 954–959, Jul. 1991.
- [7] W. Menzel, "A new traveling-wave antenna in microstrip," *Arch. Elektron. Uebertrag. Tech.*, vol. 33, no. 4, pp. 137–140, Apr. 1979.
- [8] A. A. Oliner and K. S. Lee, "The nature of the leakage from higher modes on microstrip line," in *IEEE MTT-S Int. Microw. Symp. Dig.*, Baltimore, MD, Jun. 1986, pp. 57–60.
- [9] C.-N. Hu and C.-K. C. Tzuang, "Analysis and design of large leaky-mode array employing the coupled-mode approach," *IEEE Trans. Microw. Theory Tech.*, vol. 49, no. 4, pp. 629–636, Apr. 2001.
- [10] K. C. Chen, C. K. C. Tzuang, Y. Qian, and T. Itoh, "Leaky properties of microstrip above a perforated ground plane," in *IEEE MTT-S Int. Microw. Symp. Dig.*, Anaheim, CA, Jun. 1999, pp. 69–72.
- [11] C. Caloz, T. Itoh, and A. Rennings, "CRLH metamaterial leaky-wave and resonant antennas," *IEEE Antennas Propag. Mag.*, vol. 50, no. 5, pp. 25–49, Oct. 2007.
- [12] S. Lim, C. Caloz, and T. Itoh, "Metamaterial-based electronically controlled transmission line structure as a novel leaky-wave antenna with tunable angle and beamwidth," *IEEE Trans. Microw. Theory Tech.*, vol. 53, no. 1, pp. 161–173, Jan. 2005.
- [13] F. P. Casares-Miranda, C. Camacho-Peñalosa, and C. Caloz, "High-gain active composite right/left-handed leaky-wave antenna," *IEEE Trans. Antennas Propag.*, vol. 54, no. 8, pp. 2292–2300, Aug. 2006.
- [14] J. R. James, P. S. Hall, and C. Wood, *Microstrip Antenna Theory and Design*. London, U.K.: Peregrinus, 1988.
- [15] M. Danielsen and R. Jørgensen, "Frequency scanning microstrip antennas," *IEEE Trans. Antennas Propag.*, vol. AP-27, no. 2, pp. 146–150, Mar. 1979.
- [16] J. R. James and P. S. Hall, "Microstrip antennas and arrays, part 2: New array-design technique," *Proc. Inst. Elect. Eng.—Microw., Opt., Acoust.*, vol. 1, pp. 175–181, Sep. 1977.
- [17] M. Guglielmi and D. R. Jackson, "Broadside radiation from periodic leaky-wave antennas," *IEEE Trans. Antennas Propag.*, vol. 41, no. 1, pp. 31–37, Jan. 1993.
- [18] S. Paulotto, P. Baccarelli, F. Frezza, and D. R. Jackson, "A novel technique for open-stopband suppression in 1-D periodic printed leaky-wave antennas," *IEEE Trans. Antennas Propag.*, vol. 57, no. 7, pp. 1894–1906, Jul. 2009.
- [19] A. Hessel, *Antenna Theory, Part II*, R. E. Collin and R. F. Zucker, Eds. New York: McGraw-Hill, 1969, ch. 19.
- [20] C. S. Franklin, "Improvements in wireless telegraph and telephone aerials," British Patent 242,342, Aug. 5, 1924.
- [21] N. Yang, C. Caloz, and K. Wu, "Fixed-beam frequency-tunable phase reversal coplanar stripline antenna array," *IEEE Trans. Antennas Propag.*, vol. 57, no. 3, pp. 671–681, Mar. 2009.
- [22] L. Brillouin, *Wave Propagation in Periodic Structures*. New York: Dover, 1946.
- [23] P. Baccarelli, S. Paulotto, D. R. Jackson, and A. A. Oliner, "A new Brillouin dispersion diagram for 1-D periodic printed structures," *IEEE Trans. Microw. Theory Tech.*, vol. 55, no. 7, pp. 1484–1495, Jul. 2007.
- [24] C. A. Balanis, *Antenna Theory: Analysis and Design*, 2nd ed. New York: Wiley, 1996.
- [25] S.-G. Mao, C.-W. Chiu, R.-B. Wu, and C. H. Chen, "Equivalent inducances of coplanar-stripline step discontinuities," in *Proc. Asia-Pacific Microw. Conf.*, 1997, pp. 613–616.
- [26] P. Baccarelli, C. D. Nallo, S. Paulotto, and D. R. Jackson, "A full-wave numerical approach for modal analysis of 1-D periodic microstrip structures," *IEEE Trans. Microw. Theory Tech.*, vol. 54, no. 4, pp. 1350–1362, Apr. 2006.
- [27] L. Zhu, "Guided-wave characteristics of periodic coplanar waveguides with inductive loading unit-length transmission parameters," *IEEE Trans. Microw. Theory Tech.*, vol. 51, no. 10, pp. 2133–2138, Oct. 2003.
- [28] C. H. Walter, *Traveling Wave Antennas*. New York: McGraw-Hill, 1965.
- [29] T. Kokkinos, C. D. Sarris, and G. V. Eleftheriades, "Periodic FDTD analysis of leaky-wave structures and applications to the analysis of negative-refractive-index leaky-wave antennas," *IEEE Trans. Microw. Theory Tech.*, vol. 54, no. 4, pp. 1619–1630, Apr. 2006.
- [30] D. M. Pozar, *Microwave Engineering*, 3rd ed. New York: Wiley, 2004.



Ning Yang (M'03) received the Bachelor's degree in electric engineering and Ph.D. degree in microwave engineering under a joint-program from Southeast University (SEU), Nanjing, China, and the National University of Singapore (NUS), Singapore, in 2004.

In November 2001, he became an Engineer with the Center for Wireless Communications (CWC). In 2003, he became an Associate Scientist with the Institute for Infocomm Research (I²R), Singapore. From 2005 to 2006, he was with Motorola Inc., as a Senior RF Engineer, where he was engaged in research and development of emergent RF and antenna technologies for cutting-edge mobile devices. Since October 2006, he has been a Researcher with École Polytechnique de Montréal, Montréal, QC, Canada. He has authored or coauthored over 60 peer-reviewed technical papers. One invention disclosure of his was accepted by Motorola Inc. As one of the key participants, he contributed to the development of V360, V361, V367, and ROKR E8 mobile phones of Motorola Inc. He has been a Reviewer for several transactions, journals, and letters. His current research interests include differentially integrated microwave circuits and antennas/arrays, metamaterials, substrate integrated waveguide (SIW) devices, and integrated active RF subsystems.

Dr. Yang was a Technical Program Committee (TPC) member of EuCAP'2009. He was the recipient of the Young Scientist Award of the General Assembly 2008, International Union of Radio Science (URSI) and Best Dissertation Award of 2005 by the Ministry of Education, Jiangsu, China.



Christophe Caloz (S'99–M'03–SM'06–F'10) received the Diplôme d'Ingénieur en électricité et Ph.D. degree from the École Polytechnique Fédérale de Lausanne (EPFL), Lausanne, Switzerland, in 1995 and 2000, respectively.

From 2001 to 2004, he was a Postdoctoral Research Engineer with the Microwave Electronics Laboratory, University of California at Los Angeles (UCLA). In June 2004, he joined the École Polytechnique de Montréal, Montréal, QC, Canada, where he is currently an Associate Professor, a member of the Microwave Research Center Poly-Grames, and the Holder of a Canada Research Chair (CRC). He has authored or coauthored 350 technical conference, letter and journal papers, and ten book and book chapters. He is a member of the Editorial Board of the *International Journal of Numerical Modelling* (IJNM), *International Journal of RF and Microwave Computer-Aided Engineering* (RFMiCAE), *International Journal of Antennas and Propagation* (IJAP), and *Metamaterials of the Metamorphose Network of Excellence*. He holds several patents. His research interests include all fields of theoretical, computational, and technological electromagnetics engineering with a strong emphasis on emergent and multidisciplinary topics.

Dr. Caloz is a member of the IEEE Microwave Theory and Techniques Society (IEEE MTT-S) Technical Coordinating Committee (TCC) MTT-15. He is a speaker of the MTT-15 Speaker Bureau. He is the chair of the Commission D (Electronics and Photonics) of the Canadian Union de Radio Science Internationale (URSI). He was the recipient of the 2004 UCLA Chancellor's Award for Post-doctoral Research and the 2007 IEEE MTT-S Outstanding Young Engineer Award.



Ke Wu (M'87–SM'92–F'01) is currently a Professor of electrical engineering, and Tier-I Canada Research Chair in RF and millimeter-wave engineering with the École Polytechnique de Montréal, Montréal, QC, Canada. He holds the first Cheung Kong endowed chair professorship (visiting) with Southeast University, the first Sir Yue-Kong Pao chair professorship (visiting) with Ningbo University, and an honorary professorship with the Nanjing University of Science and Technology and the City University of Hong Kong. He has been the Director of the Poly-Grames

Research Center and the founding Director of the Center for Radiofrequency Electronics Research of Quebec (Regroupement stratégique, FRQNT). He has also held guest and visiting professorship in many universities around the world. He has authored or coauthored over 730 referred papers and a number of books/book chapters. He has served on the Editorial/Review Boards of many technical journals, transactions, and letters, as well as scientific ency-

clopedias as both an editor and guest editor. He holds numerous patents. His current research interests involve substrate integrated circuits (SICs), antenna arrays, advanced computer-aided design (CAD) and modeling techniques, and development of low-cost RF and millimeter-wave transceivers and sensors for wireless systems and biomedical applications. He is also interested in the modeling and design of microwave photonic circuits and systems.

Dr. Wu is a Fellow of the Canadian Academy of Engineering (CAE) and the Royal Society of Canada (The Canadian Academy of the Sciences and Humanities). He is a member of the Electromagnetics Academy, Sigma Xi, and the URSI. He has held key positions in and has served on various panels and international committees including the chair of Technical Program Committees, International Steering Committees, and international conferences/symposia. He

will be the general chair of the 2012 IEEE Microwave Theory and Techniques Society (IEEE MTT-S) International Microwave Symposium (IMS). He is currently the chair of the joint IEEE Chapters of MTT-S/APS/LEOS, Montréal, QC, Canada. He is an elected IEEE MTT-S Administrative Committee (AdCom) member (2006–2012) and is the chair of the IEEE MTT-S Member and Geographic Activities (MGA) Committee. He is an IEEE MTT-S Distinguished Microwave Lecturer (2009–2011). He was the recipient of many awards and prizes including the first IEEE MTT-S Outstanding Young Engineer Award, the 2004 Fessenden Medal of the IEEE Canada, and the 2009 Thomas W. Eadie Medal of the Royal Society of Canada.